ceramics

MDPI

*Article*

# Preparation and Mechanical Characteristics of Multicomponent Ceramic Solid Solutions of Rare Earth Metal Oxides Synthesized by the SCS Method

**Victor Zhuravlev *, Larisa Ermakova, Rina Samigullina and Alexey Ermakov**

Institute of Solid State Chemistry, Ural Branch, Russian Academy of Sciences, 91, Pervomaiskaya, Ekaterinburg 620108, Russia; larisaer@ihim.uran.ru (L.E.); rina@ihim.uran.ru (R.S.); ermakovihim@yandex.ru (A.E.)

* Correspondence: author: zhvd@ihim.uran.ru

**Abstract:** A study into the use of the Solution Combustion Synthesis (SCS) method with glycine and citric acid to synthesize fine powders of multicomponent solid solutions of oxides of rare earth (RE) metals (Nd, Sm, Eu, Gd, Dy, and Ho) for the preparation of ceramic materials is presented. Synthesis parameters of 4-, 5-, and 6-component entropy-stabilized rare earth oxides (REOs) with a C-type cubic structure are determined. The stability of entropy-stabilized oxides (ESOs) with a C-type structure is shown to depend not only on heavy RE metal quantity, but also on the rate of heating/cooling of the samples. The temperature of the polymorphic transformation of C-type REO structures into B-type (monoclinic) or H-type (hexagonal) structural variants can be described by the equation $T\ (^{\circ}C) = 0.0214V_{cr}^{2} - 62.737V_{cr} + 46390$, where $V_{cr}$ is the unit cell volume of an oxide with a C-type structure regardless of the number of cations in the solid solution. High-temperature thermal analysis up to 1250 °C revealed that dispersed powders, which contain impurities of basic carbonates along with hydroxocarbonates of RE metals and X-ray amorphous carbon formed during SCS reactions, also react with air moisture during storage. The influence of the ESO phase and cationic composition on the morphology, porosity and microhardness of ceramics was studied. Higher-entropy oxides form samples with higher density, microhardness and a smaller size of particle agglomerates.

**Keywords:** rare earth metal oxides; solid solutions; ceramics; morphology; sintering; SCS; polymorphic transformations; microhardness



**Citation:** Zhuravlev, V.; Ermakova, L.; Samigullina, R.; Ermakov, A. Preparation and Mechanical Characteristics of Multicomponent Ceramic Solid Solutions of Rare Earth Metal Oxides Synthesized by the SCS Method. *Ceramics* **2023**, *6*, 1017–1030. https://doi.org/10.3390/ceramics6020060

Academic Editors: Elisa Torresani and Margarita A. Goldberg

Received: 24 March 2023
Revised: 14 April 2023
Accepted: 20 April 2023
Published: 22 April 2023



## 1. Introduction

Rare earth metal oxides (REOs) and their solid solutions are very important components of optical isolators and magneto-optical materials, offering high optical quality for information and communication technologies, data storage and processing elements, optics, magnetic, and laser generation [1–6]. Semiconductor films are used as dielectrics in metal oxide semiconductors due to their high dielectric constant and wide band gap ($E_g$), along with excellent physical and chemical stability when in contact with a silicon substrate [1,7]. Disposing high thermal stability, bright colors, and narrow emission bands, rare earth luminescent nanomaterials can withstand exposure to strong ultraviolet and high-energy radiation [8,9]. Among other REOs, $Y_2O_3$, $Nd_2O_3$, and $Sm_2O_3$ impart high strength and impact toughness to ceramics for various purposes [10,11], including anti-corrosion [12–14] and thermal barrier coatings [11–18]. The use of REOs as cryocoolers is another area of application. Materials based on $Gd_2O_3$ with the addition of europium exhibit an increased magnetocaloric effect. Such magnetic coolants have a high heat transfer rate and efficiency [11,19–23].

Oxides of ytterbium, terbium, europium, and samarium are included in the composition of catalysts for the selective oxidation of styrene [24], mixed $Gd_{2-x}Dy_xO_3$ are used in electrocatalysis [25], while, for catalytic smoke toxicity suppression of epoxy resin, mixed

RE oxides and yttrium are used [26]. Due to the similarity of the external electronic levels of lanthanides and yttrium, they are widely interchangeable in the crystal structures of complex oxides, allowing the complex doping of luminescent matrices, etc. However, the formation of solid solutions over the wide range of relative concentrations in binary, ternary, and more complex REO systems can be hindered by the following factors:

1. Differences in oxidation states. For example, terbium oxide under normal conditions exists in the form of $2Tb_2O_3 \cdot 3TbO_2$ (rhombohedral structure) and $2Tb_2O_3 \cdot 7TbO_2$ (triclinic structure) [27,28]. While $Tb_2O_3$ can be obtained after calcination in an inert or reducing atmosphere, it decomposes into the original oxides in air above 280 °C.

2. Crystallization of REOs in various crystal structures and the presence of polymorphism. Under ambient conditions, $CeO_2$ and $PrO_2$ oxides with a fluorite structure are formed, in the most oxidized state of which cations exist (4+). When heated, $Ln_2O_3$ oxides generally undergo several polymorphic transformations [29,30]. Three structures were identified at temperatures below 2000 °C: in the A-type hexagonal structure, lighter oxides (La–Pm); in the C-type cubic structure, oxides with smaller cation radii (Tb–Lu and Y); in medium-sized cations, Sm—Gd crystallizing in a C-type structure or in a B-type monoclinic structure [31]. At higher temperatures, transformations into hexagonal (H) and cubic (X) modifications are observed [30].

Information on phase equilibria in binary systems of REOs is most fully presented in the scientific literature for systems with the participation of $CeO_2$—$Ln_2O_3$; this may be because solid solutions with the fluorite structure have an ionic conductivity 4–5-fold higher than that of YSZ solid solutions [32]. However, since the maximum electrical conductivity was found precisely for the compositions of this range most authors limited themselves to the study of $Ce_{1-x}Ln_xO_{2-\Delta}$ materials, where x = 0–0.3 [33]. Prior to the discovery of high-entropy oxides, less attention was paid to the description of solid solutions based on REOs with a C-type structure. Table 1 presents the information obtained on binary solid solutions of REOs with a C-type crystal structure [5,9,34–39]. As a rule, these solid solutions were obtained by slow cooling after annealing at 1400 °C. The presence of $Ce^{4+}$ cations in the crystal lattice leads to the appearance of excess oxygen [34–37].

In recent years, much attention has been paid to studies of high-entropy oxides [38,40,41]. The first empirical descriptions of their structural formation were formulated: close ionic radii, mandatory nonisostructurality of one of the oxides, and the absence of complete miscibility in the binary phase diagram of at least one pair of oxides [38,41]. The general concept of entropy stabilization of the oxide system, which can be achieved by increasing the number of elements, is based on the stabilization of single-phase crystal structure by increasing the configurational entropy ($S_{conf}$) of the system [42]. Based on the maximum entropy of mixing, a higher stability of equiatomic high-temperature high-entropy oxides is postulated compared to asymmetric compositions, since, with the exception of the commensurability of the ionic radii of the cations, other factors do not offer sufficient evidentiality. According to the literature data, special techniques and techniques for synthesis and annealing are required for a number of compounds. Table 2 presents some published data on the compositions of high-entropy rare earth oxides with a C-type cubic crystal lattice.

Thus, the present article reports on the possibility of obtaining entropy-stabilized oxides (ESOs) with a non-equiatomic ratio of rare earth elements crystallizing with a C-type structure in Solution Combustion Synthesis (SCS) reactions. The dependence of the formation of single-phase oxides with a C-type structure on the content of glycine and citric acid, as well as on the annealing temperature, has been studied. The thermal behavior of single-phase powders after 700 °C has also been studied and described. Considering the morphology of powders following SCS, an attempt was made to obtain dense ESO ceramics with preservation of a C-type structure and subsequent evaluation of their mechanical properties. A new concept of designing materials already used in various fields of science and technology is based on the possibility of controlling the phase stability and functional prop-

erties of multicomponent solid solutions by controlling their configurational entropy [42]. Such studies were undertaken in the present work for entropy-stabilized oxides.

**Table 1.** Binary REOs with the C-type crystal structure.

| Compound | *a*, Å | Refs. |
|---|---|---|
| $Ce_{0.55}Eu_{0.45}O_{1.775}$ | 10.885(1) | [34] |
| $Ce_{0.50}Eu_{0.50}O_{1.75}$ | 10.886(3) | |
| $Ce_{0.45}Eu_{0.55}O_{1.725}$ | 10.886(8) | |
| $Ce_{0.40}Eu_{0.60}O_{1.70}$ | 10.886(1) | |
| $Ce_{0.30}Eu_{0.70}O_{1.65}$ | 10.887(1) | |
| $Ce_{0.25}Eu_{0.75}O_{1.625}$ | 10.886(1) | |
| $Ce_{0.20}Eu_{0.80}O_{1.60}$ | 10.884(2) | |
| $Ce_{0.10}Eu_{0.90}O_{1.55}$ | 10.883(6) | |
| $Ce_{0.50}Sm_{0.50}O_{1.75}$ | 10.914(1) | |
| $Ce_{0.40}Sm_{0.60}O_{1.70}$ | 10.917(2) | |
| $Ce_{0.30}Sm_{0.70}O_{1.65}$ | 10.920(2) | |
| $YO_{1.5}$ | 10.604(1) | [35] |
| $Ce_{0.50}Gd_{0.50}O_{1.75}$ | 10.862(2) | [36,37] |
| $Ce_{0.40}Gd_{0.60}O_{1.70}$ | 10.854(3) | |
| $Ce_{0.30}Gd_{0.70}O_{1.65}$ | 10.855(1) | |
| $Ce_{0.20}Gd_{0.80}O_{1.60}$ | 10.849(1) | |
| $Ce_{0.15}Gd_{0.85}O_{1.575}$ | 10.838(1) | |
| $Ce_{0.10}Gd_{0.90}O_{1.55}$ | 10.837(1) | |
| $Ce_{0.05}Gd_{0.95}O_{1.525}$ | 10.831(1) | |
| $[(Y_{1-x}Gd_x)_{0.99}Dy_{0.01}]_2O_3$ (x = 0 and 0.4) | 10.483–10.567 | [9] |

**Table 2.** Multicomponent solid solutions of REE oxides.

| Compound | *a*, Å | T, °C | Refs. |
|---|---|---|---|
| $Ce_{1/3}La_{1/3}$ $Nd_{1/3}Pr_{1/3}Sm_{1/3}Y_{1/3}O_{3.16}$ | 10.9652(2) | 1000 | [38] |
| $Ce_{1/3}Gd_{1/3}$ $Nd_{1/3}Pr_{1/3}Sm_{1/3}Y_{1/3}O_{3.16}$ | 10.9319(3) | | [38] |
| $Ce_{0.4}La_{0.4}$ $Pr_{0.4}Sm_{0.4}Y_{0.4}O_{3.2}$ | 10.9957(8) | 1000 | [38] |
| $Gd_{0.4}Tb_{0.4}Dy_{0.4}Ho_{0.4}Er_{0.4}O_3$ | 10.66029(8) | 1200 | [39] |
| $Ce_{0.4}La_{0.4}Pr_{0.4}Sm_{0.4}Y_{0.4}O_3$ | 10.919 | | [39] |
| $Ce_{0.5}La_{0.5}Sm_{0.5}Y_{0.5}O_{3,25}$ | 10.961 | | [39] |
| $Yb_{0.118}Lu_{0.464}Y_{1.418}O_3$ | 10.538 | 180 | [5] |
| $Ce_{2/3}Gd_{2/3}La_{2/3}O_{3.33}$ | 11.038 | 1400 | [39] |

## 2. Materials and Methods

### *2.1. Preparation and Processing of Powders*

Fine powders of multicomponent solid-solution REOs were synthesized by SCS [43,44]. The initial solutions were prepared by dissolving $RE(NO_3)_3 \cdot 6H_2O$, where RE = Nd, Sm, Eu, Gd, Dy, and Ho, in distilled water. Dual fuel was used for SCS, glycine and citric acid, with $\varphi_{citr} + \varphi_{gl} \leq 1.1$. The resulting oxide powders were calcined at 700 °C for primary burnout of expected volatile impurities, fuel residues, decompose rare earth hydroxides, and structural crystallization and form a c-type structure. To study the phase stability of

the C-type structure, successive high-temperature annealing of both powders and ceramics was carried out. The annealing temperature of 1250 °C, used both for powder annealing and ceramic sintering, is determined by the C→B transition temperature for $Gd_2O_3$. The composition of the samples, preparation conditions, and content of the C-type phase are given in Table 3.

**Table 3.** Preparation conditions, composition and weighted average ionic radius of rare earth cations, $r_{av}$.

| ESO | Composition | Fuel | | Phase C-Type, wt. % | | $r_{av}$, Å [45] |
|---|---|---|---|---|---|---|
| | | $\varphi_{gl}$ | $\varphi_{citr}$ | 700 °C | 1250 °C | |
| 1-1 | $Nd_{0.25}Sm_{0.25}Eu_{0.25}Gd_{0.25}Dy_{0.5}Ho_{0.5}O_3$ | 0.9 | 0.1 | 82.7 | | 0.9313 |
| 1-2 | | 0.8 | 0.2 | 92.2 | | |
| 1-3 | | 0.5 | 0.5 | 100 | 100 | |
| 1-4 | | 0.4 | 0.5 | 100 | 100 | |
| 2-1 | $Nd_{0.5}Sm_{0.5}Eu_{0.25}Gd_{0.25}Dy_{0.25}Ho_{0.25}O_3$ | 0.7 | 0.3 | 7.6 | | 0.9475 |
| 2-2 | | 0.5 | 0.6 | 100 | 25.6 | |
| 2-3 | | 0.5 | 0.2 | 100 | 28.0 | |
| 2-4 | | 0.4 | 0.6 | 100 | 21.9 | |
| 3 | $Nd_{0.4}Sm_{0.3}Gd_{0.4}Dy_{0.5}Ho_{0.4}O_3$ | 0.4 | 0.5 | 100 | 100 | 0.9355 |
| 4 | $Nd_{0.4}Sm_{0.2}Gd_{0.4}Dy_{0.5}Ho_{0.5}O_3$ | 0.4 | 0.5 | 99.4 | 98.3 | 0.9325 |
| 5 | $Nd_{0.4}Sm_{0.4}Gd_{0.4}Dy_{0.4}Ho_{0.4}O_3$ | 0.4 | 0.5 | 98.2 | 99.4 | 0.9380 |
| 6-1 | $Nd_{0.5}Sm_{0.5}Gd_{0.5}Dy_{0.5}O_3$ | 0.4 | 0.5 | 27.5 | | 0.9475 |
| 6-2 | | 0.5 | 0.6 | 100 | 22.4 | |
| 6-3 | | 0.4 | 0.6 | 100 | 40.4 | |

### *2.2. Preparation and Processing of Ceramics*

After annealing at 700 °C, the resulting powders were compacted on a tensile testing machine manufactured by Fritz Heckert (GDR) at a speed of movement of the object table of 4 mm/min. Compact samples in the form of disks of 2–3 mm in thickness were fabricated by dry uniaxial pressing at 8.2 GPa with following sintering at 1250 °C for 7 h in corundum crucibles. The sintering profile included the following stages: heating to 700 °C at a heating rate of 6.5°/min; heading to 1250 °C at a rate of 4.5°/min; holding at 1250 °C for 7 h; cooling to 700 °C at a rate of 3°/min; free cooling to room temperature.

The density of sintered ceramics, ρ, %, was determined from the ratio of the effective volume, $V_{ef}$, not taking into account the pore space, to the apparent volume, $V_k$, including both the solid core and the volume of closed and open pores. $V_k$ was calculated from the geometric dimensions of the sintered samples, $V_{ef}$ was measured by the pycnometric method on an AccuPyc II 1340 V1.09 helium pycnometer in a 1 $cm^3$ cuvette at a measurement error of 0.03%. The porosity, $\Phi$, was determined from relation (1).

$$\Phi = [1 - V_{ef}/V_k] * 100 \quad (1)$$

### *2.3. Characterization Techniques*

The phase composition and structure refinement of the powders and ceramics samples were performed on an XRD-7000 (Shimadzu, Japan) diffractometer using Cu Kα1 radiation in the 2θ range from 10 to 70° with a step of Δ(2θ) = 0.05° and exposure time of 3 s. Possible impurity phases were checked by comparing their XRD patterns with those in the PDF-2 database (ICDD, 2016). The unit cell parameters were refined using the POWDER CELL 2.4 software package. The microstructures of the powder and ceramic samples were characterized with a JSM 6390 LA (JEOL, Japan) scanning electron microscope (SEM).

All of the thermogravimetry (TG) and differential scanning calorimetry (DSC) curves were obtained simultaneously using a Setaram Setsys Evolution-1750 thermal analyzer in air with heating/cooling rate of 10°/min in the temperature range, ΔT, 20–1250 °C. The microhardness of ESO ceramics was measured using a Micromet 1 microhardness tester (Buehler LTD. Lake Bluff, Illinois, USA) with automatic diamond pyramid indentation under a load of 100 g and a load time of 10 s. From the data obtained by performing at least 10 measurements of microhardness (indentations of a diamond pyramid) on each sample, where both diagonals were measured on each print, the average value of microhardness was determined and the measurement error was estimated.

## 3. Results and Discussion

### *3.1. Dispersed Solid Solutions of Rare Earth Metal Oxides*

The production of multicomponent oxides of rare earth metals with a C-type structure using the SCS method implies the selection of a fuel such that the combustion process does not develop a temperature at which the formation of the monoclinic B form begins. By carrying out the synthesis under various conditions, it was possible to experimentally establish the ratio of glycine and citric acid, comprising the most universal ratio for the synthesis of the studied systems with the desired cubic structure. Table 3 shows that an increase in the relative content of glycine in the fuel contributes to an increase in the time of fire activation, as well as increasing the exothermicity of the reaction; the precursors ESO-1-1, ESO-1-2 and ESO-2-1 contain noticeable amounts of the monoclinic phase following heat treatment at 700 °C. The predominance of citric acid in the fuel composition reduces the synthesis temperature and the degree of crystallinity of the products under such conditions, as well as promoting the formation of the C-type phase.

In addition to the synthesis conditions, the formation of the C-type structure is affected by the weighted average ionic radius of the incoming cations [46]. An REO with a smaller cationic ionic radius than gadolinium crystallizes in the cubic C-type. The stability of the cubic structure of C-type for $NdO_{1.5}$ is limited by a temperature of 590 °C, 860 °C for $SmO_{1.5}$, and 1060 °C for $EuO_{1.5}$. Based on the obtained data, inclusion in the composition of samples of rare earth element (REE) cations with a radius greater than that of gadolinium in an amount > 50 at. % prevents the formation of entropy-stabilized C-type oxides. In particular, a relative content of the $Nd^{3+}$ cation in the crystal lattice of ESO samples in the range of 12.5–20% does not prevents the formation of a cubic structure. All samples of ESO-1—ESO-6 obtained in combustion reactions at a certain ratio of glycine and citric acid demonstrated a cubic structure after annealing at 700 °C, as well as retaining it after cooling. The change in the upper temperature limit of the region of existence of the C-type structure can be more accurately traced by the change in the volume of the crystal cell depending on the type of REE (Figure 1). The figure is constructed on the basis of data on the structural phase transitions of rare earth oxides [29,47] and unit cell volumes $V_{cr}$ for cubic structures of REOs taken from the PDF-2 database (ICDD, 2016).

This dependence can be written by Equation (2) with reliability $R^2 = 0.9775$:

$$T, ^\circ C = 0.0214 V_{cr}^2 - 62.737 V_{cr} + 46390 \quad (2)$$

The temperatures of the upper limit of stability of ESO samples with a C-type structure, calculated using Equation (2), are presented in Table 4.

The calculated transition temperatures C→B(H) are consistent with the data of X-ray diffraction analysis of the samples. As the X-ray phase analysis showed, only ESO-1-3, ESO-1-4, and ESO-3 samples retain the C-type structure up to 1250 °C (Figure 2), while, for the remaining ESO samples (Table 3), the upper stability temperature C-type structures appear below. For example, for ESO-2-3, the appearance of a monoclinic phase is observed already after annealing at 800 °C (Figure 3). The mass fraction of the C-type phase of ESO samples after annealing at 1250 °C is given in Table 3. As can be seen, the synthesis parameters (the ratio of glycine and citric acid) have a significant effect on the phase composition of ESO samples. We will consider these patterns in our next article.

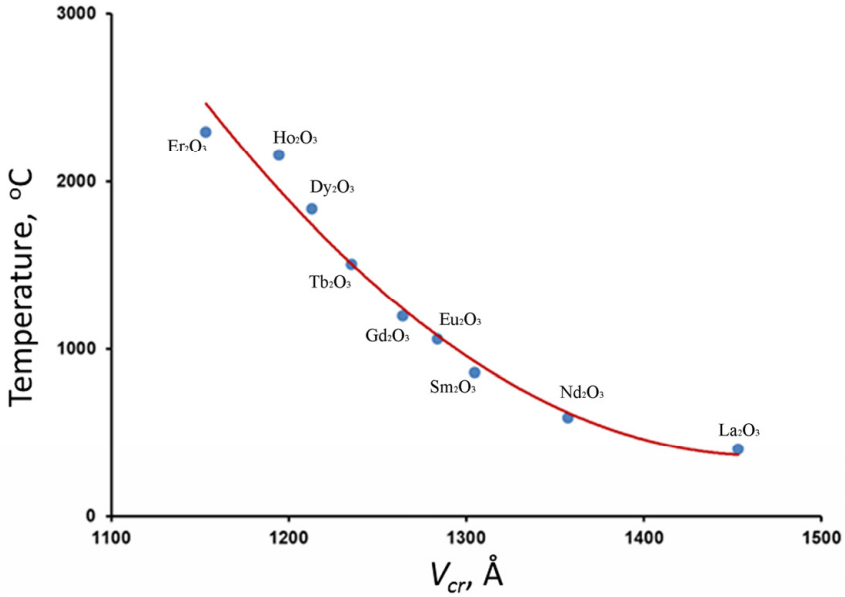


**Figure 1.** Dependence of the change in the temperatures of the C→B(H) rare earth metal oxide polymorphic transition on $V_{cr}$.

**Table 4.** Temperatures of polymorphic transitions C→B(H) for ESOs.

| ESO | Composition | a, Å | T, °C C→B(H) |
|---|---|---|---|
| 1-4 | $Nd_{0.25}Sm_{0.25}Eu_{0.25}Gd_{0.25}Dy_{0.5}Ho_{0.5}O_3$ | 10.787(1) | 1313 |
| 2-3 | $Nd_{0.5}Sm_{0.5}Eu_{0.25}Gd_{0.25}Dy_{0.25}Ho_{0.25}O_3$ | 10.881(1) | 993 |
| 3 | $Nd_{0.4}Sm_{0.3}Gd_{0.4}Dy_{0.5}Ho_{0.4}O_3$ | 10.795(1) | 1282 |
| 6-3 | $Nd_{0.5}Sm_{0.5}Gd_{0.5}Dy_{0.5}O_3$ | 10.878(1) | 1002 |

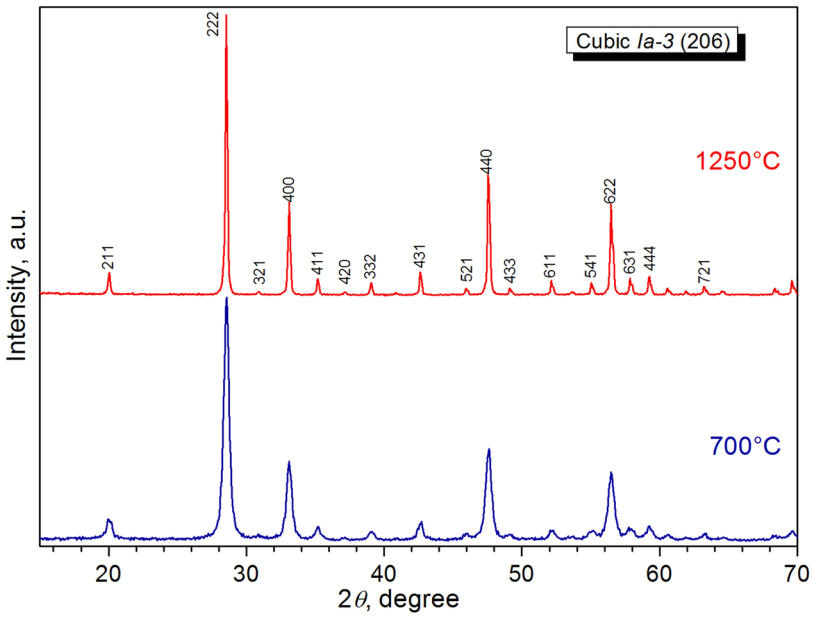


**Figure 2.** In situ X-ray diffraction patterns of the ESO-1-4 sintered at various temperatures.

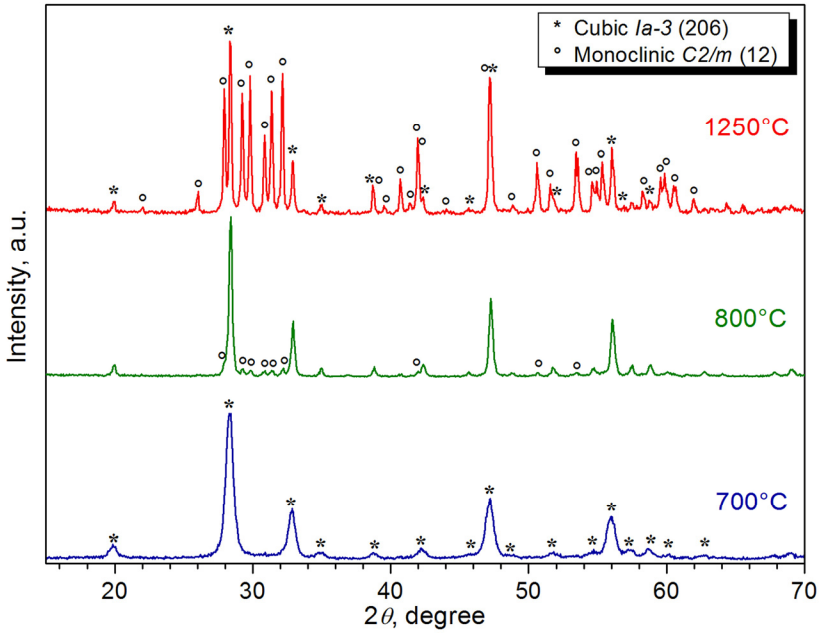


**Figure 3.** In situ X-ray diffraction patterns of the ESO-2-3 sintered at various temperatures.

There are no thermal effects that could be attributed to polymorphic transformations shown on the DSC curves of dispersed powders ESO-1-2 and ESO-2-3 on the heating and cooling curves in the range of 100–1250 °C (Figure 4a,b). It follows from this that cubic ESO-1-2 and ESO-2-3 are stable over a wider temperature range than the simple oxides of neodymium and samarium included in their composition. The appearance of an exo-effect on the DSC curve of the ESO-1-2 sample associated with the presence of a carbon impurity is explained below.

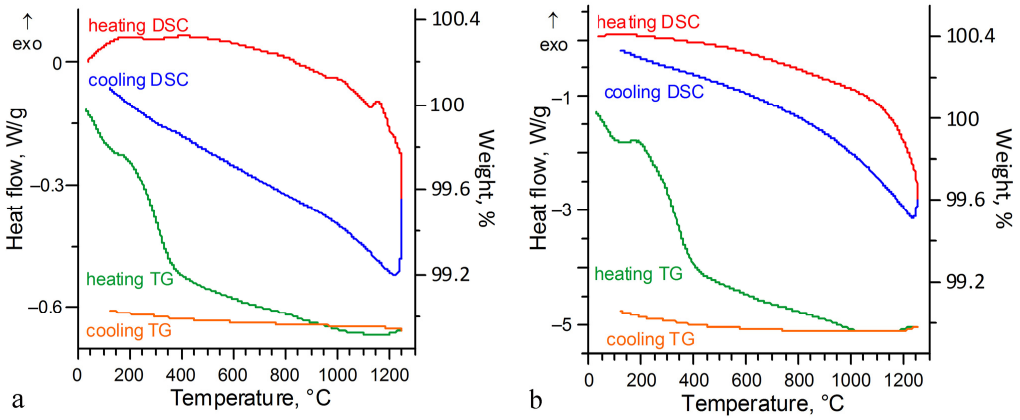


**Figure 4.** DSC and TG heating and cooling curves of: (**a**) ESO-1-2 and (**b**) ESO-2-3.

The X-ray diffraction data of a ceramic sample ESO-2-3 contradict the thermogram of the powder of this composition: it is two-phase after 1250 °C and contains 72 wt. % monoclinic phase (type B). It can be assumed that the sample does not have time to complete the C→B transition during thermal analysis (at a heating rate of 10°/min); however, in the ESO powders that underwent 7-h annealing in a furnace at 1250 °C, this process is completed. The two-phase nature of ESO-2-3 after cooling in a furnace also speaks in favor of a low rate of polymorphic transformation. After 7 h of annealing at 1250 °C, ceramic samples ESO-4, ESO-5, ESO-6 also decompose; however, in the first two, the amount of the monoclinic phase is small, while ESO-3 remains monophasic.

TG-DSC analysis of ESO samples obtained by the SCS method and annealed at 800 °C in air revealed the presence of impurities in an amount of 0.43–1.53 wt. %, which are removed upon heating (Table 5, Figure 5a–d). Similar effects were described by Shlyakhtina A.V. et al. [48] in their complex analysis (DSC–TG, XRF, IR and Raman spectroscopy) of obtaining ceramics $Nd_2O_3$+2$HfO_2$ and $Dy_2O_3$-2$HfO_2$. These were identified as decomposition products of basic REE carbonates and hydroxocarbonates in the range of 250–600 °C and of X-ray amorphous carbon in the range of 750–1200 °C [48]. In our opinion, the presence of exo-effects on the DSC curve in the range of 800–1250 °C confirms the oxidation of amorphous carbon formed from citric acid under combustion conditions.

**Table 5.** ESO weight change during thermal analysis.

| ESO | Composition | −ΔP, % | ΔT, °C | +ΔP, % | Exo-Effect Temperature T, °C |
|---|---|---|---|---|---|
| 1-2 | $Nd_{0.25}Sm_{0.25}Eu_{0.25}Gd_{0.25}Dy_{0.5}Ho_{0.5}O_3$ | 0.9 | 20–1100 | | 1154; 1205 |
| 1-4 | | 0.85 | 20–1250 | | 1074; 1197 |
| 2 | $Nd_{0.5}Sm_{0.5}Eu_{0.25}Gd_{0.25}Dy_{0.25}Ho_{0.25}O_3$ | 0.99 | 20–1025 | | |
| 3 | $Nd_{0.4}Sm_{0.3}Gd_{0.4}Dy_{0.5}Ho_{0.4}O_3$ | 0.52 | 20–800 | 0.18 | 953; 1163 |
| 4 | $Nd_{0.4}Sm_{0.2}Gd_{0.4}Dy_{0.5}Ho_{0.5}O_3$ | 0.43 | 20–800 | 0.04 | 856; 1101 |
| 5 | $Nd_{0.4}Sm_{0.4}Gd_{0.4}Dy_{0.4}Ho_{0.4}O_3$ | 0.88 | 20–1250 | | 1246 |
| 6-2 | $Nd_{0.5}Sm_{0.5}Gd_{0.5}Dy_{0.5}O_3$ | 1.53 | 20–1250 | | 996; 1092 |

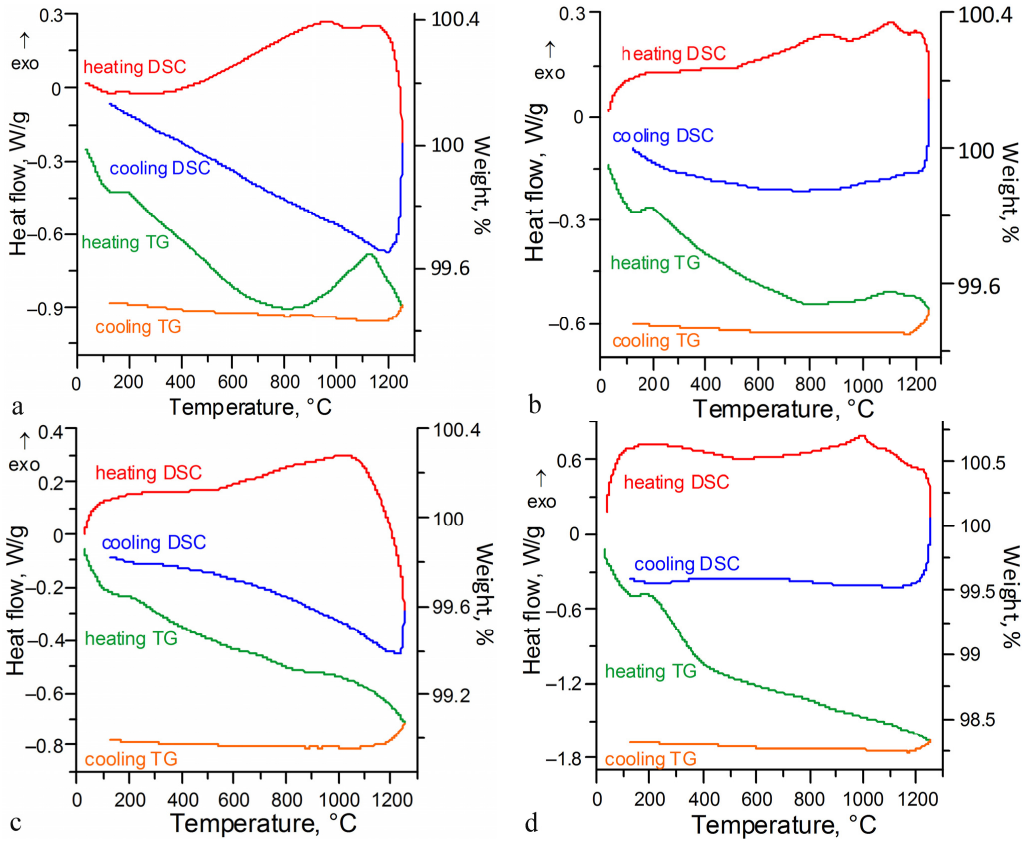


**Figure 5.** DSC and TG heating and cooling curves of: (**a**) ESO-3, (**b**) ESO-4, (**c**) ESO-5, and (**d**) ESO-6-2.

On TG and DSC curves of samples ESO-3 and ESO-4 in the region 800–1100 °C (Figure 5a,b), the gravimetric curve fixes a weight gain (+ΔP) of 0.04–0.018% (Table 5). It can be assumed that this is due to the oxidation of either $Sm^{2+}$ cations or REE carbides,

whose formation is quite possible, since the ESO-3 and ESO-4 samples were obtained in a more reducing (as compared to other ESOs) medium (see Table 3).

Carbon impurities often present in the products of SCS reactions [43] due to various modifications can be oxidized or decomposed only at high temperatures [44]. These assumptions explain the observed exo-effects on the DSC curves of all ESO samples, whose heating is also accompanied by a decrease in mass (−ΔP) (Table 5).

Such interpretations of the results of thermal analysis are supported by an additional experiment performed by the authors. Figure 6 shows the results of TG—DSC analysis of sample ESO-1-4 after synthesis and annealing at 800 °C (blue and green lines) and repeated thermal analysis of sample ESO-1-4 after annealing at 1250 °C.

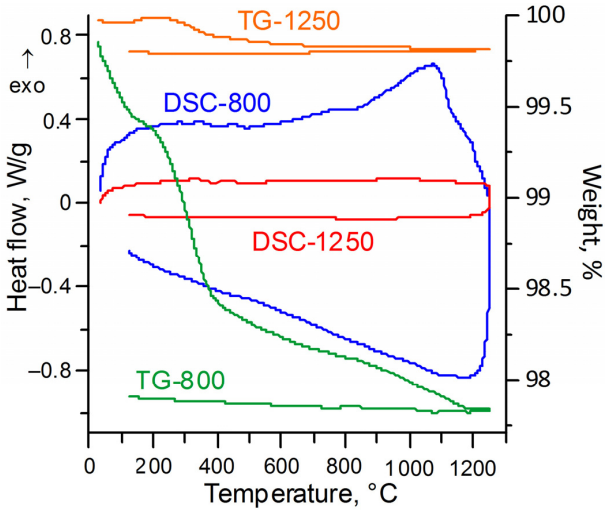


**Figure 6.** DSC and TG heating and cooling curves of ESO-1-4 after synthesis and annealing at 800 °C (blue and green curves) and after annealing at 1250 °C (red and orange curves).

The powder can be seen to lose up to 0.41% following synthesis, annealing at 800 °C and storage in air; the thermogram shows a blurred exo-effect with a maximum at 1074 °C, which is accompanied by a significant weight loss in the amount of 1.6% up to 1200 °C. During cooling, there is no change in the mass of the sample and no thermal effects. Repeated DSC of this sample annealed at 1250 °C shows no weight loss and no corresponding thermal effects both on heating and on cooling. This proves the removal of volatile impurities and the absence of polymorphic transformations at a heating/cooling rate of 10 °C/min.

### *3.2. Ceramic Solid Solutions of Rare Earth Metal Oxides*

Along with the heat treatment conditions on the microstructure and physical and mechanical properties of ceramics, the influence of the ESO composition was studied on samples of dense ceramics obtained by firing samples in the form of tablets at a temperature of 1250 °C. The indicators of relative density, open porosity, as well as the micro-structure and microhardness of ceramics were evaluated.

The morphology of the powders used to manufacture ceramics determines its sinterability and density. The particle size and distribution, as well as the presence and shape of agglomerates, have a significant effect on both the consolidation of the powder and the microstructure of the sintered ceramic. In turn, the powder morphology is determined by the SCS parameters. The gases released during the combustion reaction, as well as during annealing at 700 °C, when the carbon-containing fuel residues are decomposed, loosen the reaction mass. However, the presence of glycine in the fuel composition increases the duration of fire retention, leading to the formation of agglomerates in which the particles are chemically bonded to each other. As shown in Figure 7a–c, the powders have a submicron particle size (less than 1 μm) following annealing at 700 °C. During annealing of the ESO-1-4 and ESO-2-3 powders at 1250 °C, coarsening of particles is observed due to

sintering of smaller particles; although their size still does not exceed 1 μm, the shape of the particles becomes rounded (Figure 7d,e). As in ESO-6-2, the observed agglomerates are larger and denser and more consolidated (Figure 7f). The agglomeration presence can lead to an uneven distribution of the packing density of powder particles in the compact and consequent inhomogeneous sintering of various pressing areas.

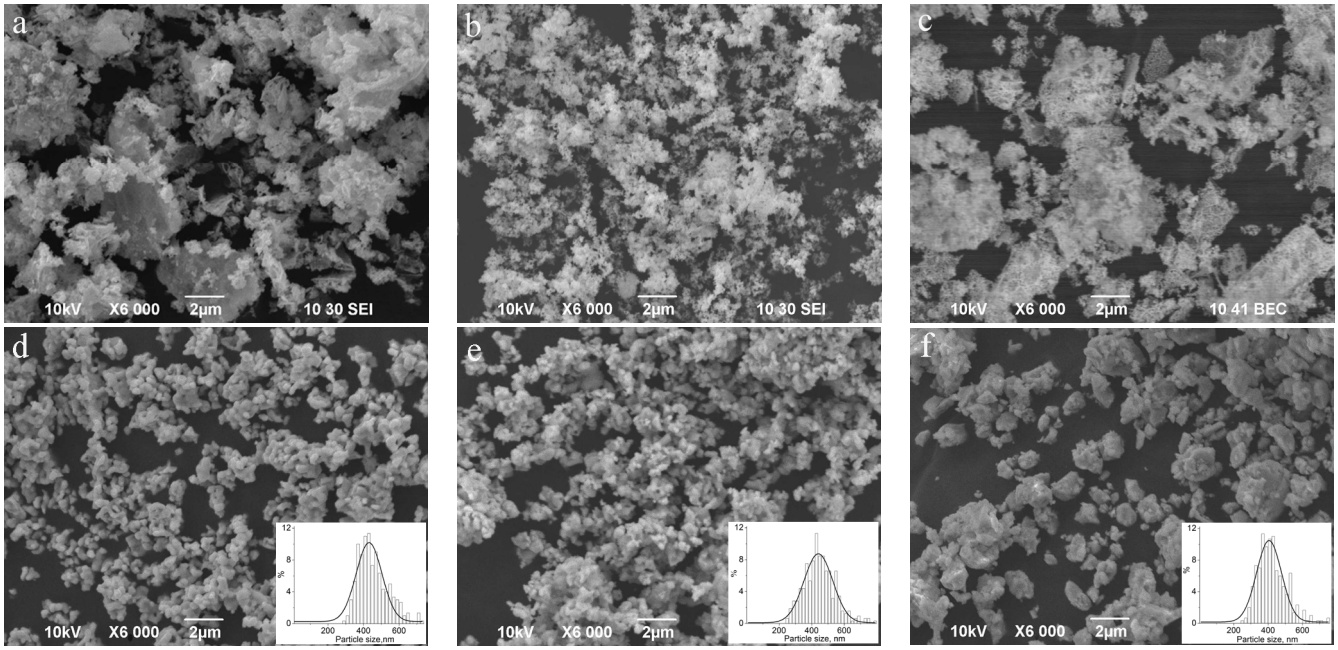


**Figure 7.** SEM images of the morphology of powder samples sintered at 700 and 1250 °C, respectively: (**a**,**d**) ESO-1-4, (**b**,**e**) ESO-2-3, and (**c**,**f**) ESO-6-2.

Studies of the microstructure of ceramic surfaces carried out under similar conditions for the preparation of both powders and tablets, show that ceramics from 6-cationic ESO-1-4 and ESO-2-3 are characterized by smaller particles in close contact with each other and with pronounced boundaries; these are uniform in shape and size from 0.2 to 1.4 μm (Figure 8a,b). With a decrease in the number of cations to 5 in a monophasic C-type structure ESO-3, the aggregate sizes increase (Figure 8c); however, an increase in the specific holmium cation content and a decrease in the amount of the $Sm^{3+}$ cation in the ESO-4 crystal lattice gives the ceramics a denser packing and some reduction in grain size (Figure 8d). The disintegration of the monophasic sample ESO-6-2 after sintering at 1250 °C and the appearance of a significant amount of a phase with a monoclinic structure (Table 3) is accompanied by the formation of elongated particles and an increase in their size in length up to 3 μm (Figure 8f). As a result, the porosity of ceramics increases significantly (Table 6). In addition, the transition from low- and medium-entropy oxides (ESO-6, ESO-3) to high-entropy oxides (ESO-1, ESO-2) correlates with an increase in the relative density of samples upon pressing (Table 6).

The resulting samples of ESO ceramics are characterized by microhardness values in the range from 2.6 to 5.7 GPa (Table 6), whose fluctuations are mainly due to differences in the microstructure of the samples. The microhardness of ceramics obtained by the same method is determined both by a smaller average particle size of the initial powder (as in the case of ESO-1-4 and ESO-2-3) and a higher sintering process intensity (ESO-5). In addition, a correlation between the ceramic microhardness and its relative density is recorded (Table 6). The highest values of microhardness were found in high-entropy samples ESO-1 (monophase) and ESO-2 (dual phase). While it is generally accepted that high-entropy ceramics should be principally single phase, dual-phase high-entropy ceramics are recently included in this family of materials [42].

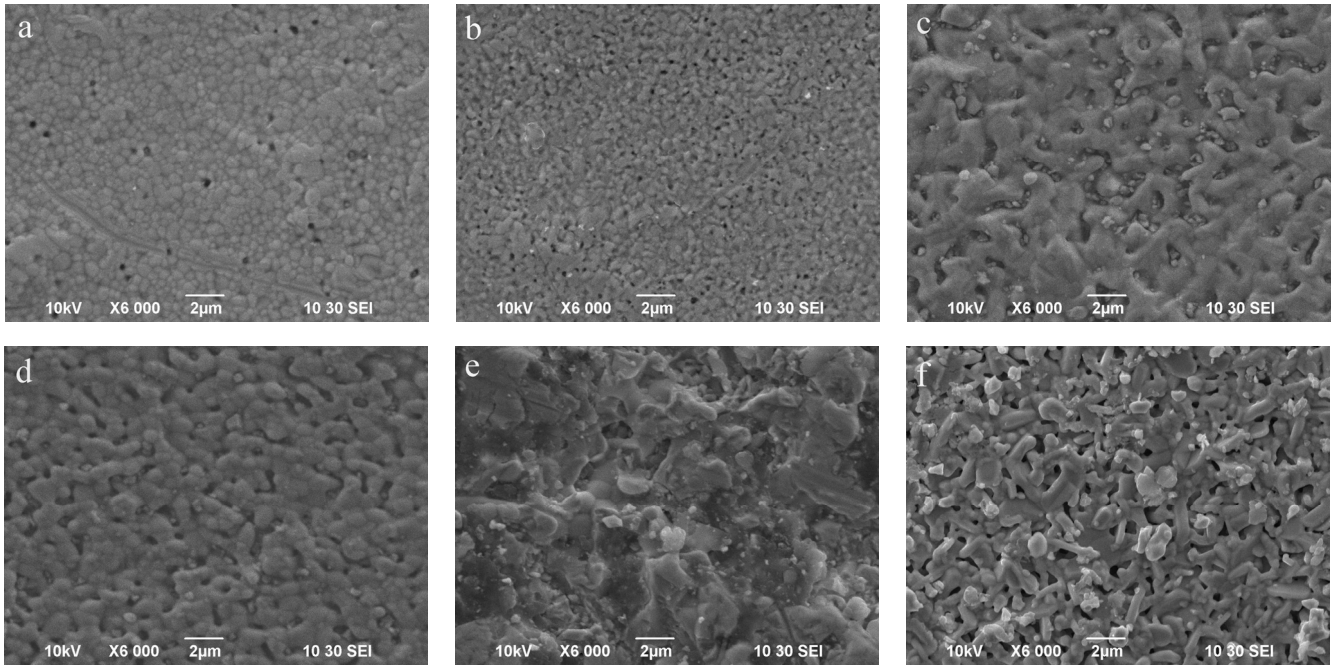


**Figure 8.** SEM images of the surface morphology of the ceramic samples sintered at 1250 °C: (**a**) ESO-1-4, (**b**) ESO-2-3, (**c**) ESO-3, (**d**) ESO-4, (**e**) ESO-5 and (**f**) ESO-6-2.

**Table 6.** Density $\rho$, porosity $\phi$ and microhardness of ESO ceramics.

| ESO | Composition | $\rho$, % | $\phi$, % | $H_v$, GPa |
|---|---|---|---|---|
| 1-3 | $Nd_{0.25}Sm_{0.25}Eu_{0.25}Gd_{0.25}Dy_{0.5}Ho_{0.5}O_3$ | 79.9 | 20.1 | 3.5 |
| 1-4 | | 92.6 | 7.4 | 5.1 |
| 2-2 | $Nd_{0.5}Sm_{0.5}Eu_{0.25}Gd_{0.25}Dy_{0.25}Ho_{0.25}O_3$ | 75.9 | 24.1 | 4.4 * |
| 2-3 | | 92.2 | 7.8 | 5.3 * |
| 3 | $Nd_{0.4}Sm_{0.3}Gd_{0.4}Dy_{0.5}Ho_{0.4}O_3$ | 71.9 | 28.1 | 4.5 |
| 4 | $Nd_{0.4}Sm_{0.2}Gd_{0.4}Dy_{0.5}Ho_{0.5}O_3$ | 64.8 | 35.2 | 2.6 |
| 5 | $Nd_{0.4}Sm_{0.4}Gd_{0.4}Dy_{0.4}Ho_{0.4}O_3$ | 78.4 | 21.6 | 5.7 |
| 6-2 | $Nd_{0.5}Sm_{0.5}Gd_{0.5}Dy_{0.5}O_3$ | 69.0 | 31.0 | 3.1 * |
| 6-3 | | 69.7 | 30.3 | 3.8 * |

*—mixture of cubic and monoclinic phases.

## 4. Conclusions

Six mixed, entropy-stabilized REOs were obtained by SCS reactions with glycine and citric acid. By replacing glycine with citric acid to reduce the temperatures of the synthesis process, it becomes possible to obtain solid solutions of oxides of neodymium, europium, samarium, gadolinium, dysprosium, and holmium in the C-type crystal structure after annealing at 700 °C. It has been established that the maximum temperatures of the polymorphic transformation of 4-, 5- and 6-cationic ESOs, as well as those of simple REOs, increase with a decrease in the volume of the elementary crystal lattice and can be described by a second-degree equation. The obtained data on X-ray phase and DSC analysis of dispersed ESOs indicate a low rate of mutual polymorphic transformations of polycationic oxides C $\leftrightarrow$ B(H).

Dispersed ESOs are prone to sorption of water vapor during storage with the formation of hydroxides, carbonates, hydroxocarbonates. Under reducing conditions, SCS is accompanied by the formation of carbon impurities or rare earth metal carbides in low-entropy ESOs, as well as, presumably, by partial reduction of $Sm^{3+}$ cations to $Sm^{2+}$.

Ceramic ESOs with a C-type structure with 6 cations in the crystal lattice form denser samples compared to 4-cation and composite oxides. The microhardness of the ceramic also increases when increasing the number of heavy rare earth elements in the composition of the ESO.

**Author Contributions:** Conceptualization, data curation, project administration, supervision, writing—original draft, and writing—review and editing, V.Z.; formal analysis, investigation, methodology, visualization, writing—original draft, and writing—review and editing, L.E.; formal analysis, investigation, methodology, visualization, and writing—review and editing, R.S.; formal analysis, investigation, and methodology, A.E. All authors have read and agreed to the published version of the manuscript.

**Funding:** This research received no external funding. The work was carried out in accordance with the state assignment and R&D plans of ISSC UB RAS: AAAA–A19–119031890026–6 and AAAA-A19-119031890025-9.

**Conflicts of Interest:** The authors declare no conflict of interest.

## References

1. Patil, A.S.; Patil, A.V.; Dighavkar, C.G.; Adole, V.A.; Tupe, U.J. Synthesis techniques and applications of rare earth metal oxides semiconductors: A review. *Chem. Phys. Lett.* **2022**, *796*, 139555. [CrossRef]
2. Furuse, H.; Yasuhara, R. Magneto-optical characteristics of holmium oxide ($Ho_2O_3$) ceramics. *Opt. Mater. Express* **2017**, *7*, 827–833. [CrossRef]
3. Snetkov, I.L.; Yakovlev, A.I.; Permin, D.A.; Balabanov, S.S.; Palashov, O.V. Magnetooptical Faraday effect in dysprosium oxide ($Dy_2O_3$) based ceramics obtained by vacuum sintering. *Opt. Lett.* **2018**, *43*, 4041–4044. [CrossRef] [PubMed]
4. Dai, J.W.; Li, J. Promising magneto-optical ceramics for high power Faraday isolators. *Scr. Mater.* **2018**, *155*, 78–84. [CrossRef]
5. Maksimov, R.N.; Yurovskikh, A.S.; Shitov, V.A. Fabrication, Microstructure, and Spectroscopic Properties of Transparent $Yb_{0.118}Lu_{0.464}Y_{1.418}O_3$ Ceramics. *Phys. Status Solidi* **2020**, *217*, 1900883. [CrossRef]
6. Permin, D.A.; Balabanov, S.S.; Novikova, A.V.; Snetkov, I.L.; Palashov, O.V.; Sorokin, A.A.; Ivanov, M.G. Fabrication of Yb-doped $Lu_2O_3$-$Y_2O_3$-$La_2O_3$ solid solutions transparent ceramics by self-propagating high-temperature synthesis and vacuum sintering. *Ceram. Int.* **2019**, *45*, 522–529. [CrossRef]
7. Shuan, L.; Lin, Y.; Tang, S.; Feng, L.; Li, X. A review of rare-earth oxide films as high *k* dielectrics in MOS devices. *J. Rare Earths* **2021**, *39*, 121–128. [CrossRef]
8. Filho, P.C.S.; Lima, J.F.; Serra, O.A. From lighting to photoprotection: Fundamentals and applications of rare earth materials. *J. Braz. Chem. Soc.* **2015**, *26*, 2471–2495. [CrossRef]
9. Lu, B.; Sun, Z.G.; Wang, X.Y.; Chen, H.B.; Sakka, Y.; Li, J.-G. Photoluminescent and scintillant properties of highly transparent $[(Y_{1-x}Gd_x)_{0.99}Dy_{0.01}]_2O_3$ (x = 0 and 0.4) ceramics. *J. Am. Ceram. Soc.* **2019**, *102*, 4773–4780. [CrossRef]
10. Balaram, V. Rare earth elements: A review of applications, occurrence, exploration, analysis, recycling, and environmental impact. *Geosci. Front.* **2019**, *10*, 1285–1303. [CrossRef]
11. Hossain, M.K.; Rubel, M.H.K.; Akbar, M.A.; Hafez Ahmed, M.H.; Haque, N.; Rahman, M.F.; Hossain, J.; Hossain, K.M. A review on recent applications and future prospects of rare earth oxides in corrosion and thermal barrier coatings, catalysts, tribological, and environmental sectors. *Ceram. Int.* **2022**, *48*, 32588–32612. [CrossRef]
12. Tan, Y.; Liao, W.; Zeng, S.; Jia, P.; Teng, Z.; Zhou, X.; Zhang, H. Microstructures, thermophysical properties and corrosion behaviours of equiatomic five-component rare-earth monosilicates. *J. Alloys Compd.* **2022**, *907*, 164334. [CrossRef]
13. Singh, A.K.; Kutty, T.R.G.; Sinha, S. Pulsed laser deposition of corrosion protective Yttrium Oxide ($Y_2O_3$) coating. *J. Nucl. Mater.* **2012**, *420*, 374–381. [CrossRef]
14. Guergova, D.; Stoyanova, E.; Stoychev, D.; Avramova, I.; Stefanov, P. Self-healing effect of ceria electrodeposited thin films on stainless steel in aggressive 0.5 mol/L NaCl aqueous solution. *J. Rare Earths* **2015**, *33*, 1212–1227. [CrossRef]
15. Guo, L.; Li, M.; Ye, F. Phase stability and thermal conductivity of $RE_2O_3$ (RE=La, Nd, Gd, Yb) and $Yb_2O_3$ co-doped $Y_2O_3$ stabilized $ZrO_2$ ceramics. *Ceram. Int.* **2016**, *42*, 7360–7365. [CrossRef]
16. Bahamirian, M.; Hadavi, S.M.M.; Farvizi, M.; Rahimipour, M.R.; Keyvani, A. Phase stability of $ZrO_2$ 9.5$Y_2O$ 5.6$Yb_2O_3$ 5.2$Gd_2O_3$ compound at 1100 °C and 1300 °C for advanced TBC applications. *Ceram. Int.* **2019**, *45*, 7344–7350. [CrossRef]
17. Jeon, H.; Lee, I.; Oh, Y. Changes in high-temperature thermal properties of modified YSZ with various rare earth doping elements. *Ceram. Int.* **2022**, *48*, 8177–8185. [CrossRef]
18. Zhang, D.; Yu, Y.; Feng, X.; Tian, Z.; Song, R. Thermal barrier coatings with high-entropy oxide as a top coat. *Ceram. Int.* **2022**, *48*, 1349–1359. [CrossRef]

19. Krishnaiah, K.V.; Rajeswari, R.; Kumar, K.U.; Babu, S.S.; Martín, I.R.; Jayasankar, C.K. Spectroscopy and radiation trapping of $Yb^{3+}$ ions in lead phosphate glasses. *J. Quant. Spectrosc. Radiat. Transf.* **2014**, *140*, 37–47. [CrossRef]
20. Hazarika, S.; Behera, P.S.; Mohanta, D.; Nirmala, R. Magnetocaloric effect of $Gd_2O_3$ nanorods with 5% Eu-substitution. *Appl. Surf. Sci.* **2019**, *491*, 779–783. [CrossRef]
21. Arun, B.; Akshay, V.R.; Mutta, G.R.; Venkatesh, C.; Vasundhara, M. Mixed rare earth oxides derived from monazite sand as an inexpensive precursor material for room temperature magnetic refrigeration applications. *Mater. Res. Bull.* **2017**, *94*, 537–543. [CrossRef]
22. Li, C.L.; Zheng, S.S.; Barasa, G.O.; Zhao, Y.F.; Wang, L.; Wang, C.L.; Lu, Y.; Qiu, Y.; Cheng, J.B.; Luo, Y.S. A comparative study on magnetic behaviors and magnetocaloric effect in heavy rare-earth antiferromagnetic orthoferrites $RFeO_3$ (R = Dy, Ho and Er). *Ceram. Int.* **2021**, *47*, 35160–35169. [CrossRef]
23. Zelěnáková, A.; Hrubovćák, P.; Berkutova, A.; Šofranko, O.; Kučerka, N.; Ivankov, O.; Kuklin, A.; Girman, V.; Zelěnčk, V. Gadolinium-oxide nanoparticles for cryogenic magnetocaloric applications. *Sci. Rep.* **2022**, *12*, 2282. [CrossRef]
24. Patil, N.S.; Uphade, B.S.; Jana, P.; Bhargava, S.K.; Choudhary, V.R. Epoxidation of styrene by *t*-butyl hydroperoxide over gold supported on $Yb_2O_3$ and other rare earth oxides. *Chem. Lett.* **2004**, *33*, 400–401. [CrossRef]
25. Behnamfar, M.T.; Hadadzadeh, H.; Akbarnejad, E.; Allafchian, A.R.; Assefi, M.; Khedri, N. Electrocatalytic reduction of $CO_2$ to CO by Gd(III) and Dy(III) complexes; and $M_2O_3$ nanoparticles (M = Gd and Dy). *J. CO2 Util.* **2016**, *13*, 61–70. [CrossRef]
26. Wang, J.; Qiu, S.; Cheng, L.; Chen, W.; Zhou, Y.; Zou, B.; Han, L.; Xu, Z.; Yang, W.; Hu, Y.; et al. Synergistic effects of aryl diazonium modified Few-Layer black Phosphorus/Ultrafine rare earth yttrium oxide with enhancing flame retardancy and catalytic smoke toxicity suppression of epoxy resin. *Appl. Surf. Sci.* **2022**, *571*, 151356. [CrossRef]
27. Balabanov, S.S.; Permin, D.A.; Rostokina, E.Y.; Egorov, S.V.; Sorokin, A.A.; Kuznetsov, D.D. Synthesis and structural characterization of ultrafine terbium oxide powders. *Ceram. Int.* **2017**, *43*, 16569–16574. [CrossRef]
28. Zhang, J.; Von Dreele, R.; Eyring, L. The structures of $Tb_7O_{12}$ and $Tb_{11}O_{20}$. *J. Solid State Chem.* **1993**, *104*, 21–32. [CrossRef]
29. Traverse, J.P. Etude du Polymorphism des Sesquioxides de Terres Rares. Ph.D. Thesis, L'Univérsite Scientifique et Medicale de Grenoble, Grenoble, France, 1971; 150p.
30. Foex, M.; Traverse, J.P. Remarques sur les transformation cristalines presentees a hautes temperature par les sesquioxides de terres rares. *Rev. Intern. Hautes Temper. Refract.* **1966**, *3*, 429–453.
31. Adachi, G.-Y.; Imanaka, N. The binary rare earth oxides. *Chem. Rev.* **1998**, *98*, 1479–1514. [CrossRef]
32. Kharton, V.V.; Figueiredo, F.M.; Navarro, L.; Naumovich, E.N.; Kovalevsky, A.V.; Yaremchenko, A.A.; Viskup, A.P.; Carneiro, A.; Marques, F.M.B.; Frade, J.R. Ceria-based materials for solid oxide fuel cells. *J. Mater. Sci.* **2001**, *36*, 1105–1117. [CrossRef]
33. Mogensen, M.B.; Sammes, N.M.; Tompsett, G.A. Physical, chemical and electrochemical properties of pure and doped ceria. *Solid State Ionics* **2000**, *129*, 63–94. [CrossRef]
34. Mandal, B.P.; Grover, V.; Tyagi, A.K. Phase relations, lattice thermal expansion in $Ce_{1-x}Eu_xO_{2-x/2}$ and $Ce_{1-x}Sm_xO_{2-x/2}$ systems and stabilization of cubic $RE_2O_3$ (RE: Eu, Sm). *Mater. Sci. Eng.* **2006**, *430*, 120–124. [CrossRef]
35. Chavan, S.V.; Mathews, M.D.; Tyagi, A.K. Phase Relations and Thermal Expansion Studies in the Ceria–Yttria System. *J. Am. Ceram. Soc.* **2004**, *87*, 1977–1980. [CrossRef]
36. Grover, V.; Tyagi, A.K. Phase relations, lattice thermal expansion in $CeO_2$–$Gd_2O_3$ system, and stabilization of cubic gadolinia. *Mater. Res. Bull.* **2004**, *39*, 859–866. [CrossRef]
37. Grover, V.; Achary, S.N.; Tyagi, A.K. Structural analysis of excess-anion C-type rare earth oxide: A case study with $Gd_{1-x}Ce_xO_{1.5+x/2}$ (x = 0.20 and 0.40). *J. Appl. Cryst.* **2003**, *36*, 1082–1084. [CrossRef]
38. Djenadic, R.; Sarkar, A.; Clemens, O.; Loho, C.; Botros, M.; Chakravadhanula, V.S.; Kübel, C.; Bhattacharya, S.S.; Ashutosh, S.; Gandhi, A.S.; et al. Multicomponent equiatomic rare earth oxides. *Mater. Res. Lett.* **2017**, *5*, 102–109. [CrossRef]
39. Pianassola, M.; Loveday, M.; McMurray, J.W.; Koschan, M.; Melcher, C.L.; Zhuravleva, M. Solid-state synthesis of multicomponent equiatomic rare-earth oxides. *J Am Ceram Soc.* **2020**, *103*, 2908–2918. [CrossRef]
40. Gild, J.; Samiee, M.; Braun, J.L.; Harrington, T.; Vega, H.; Hopkins, P.E.; Vecchio, K.; Luo, J. High-entropy fluorite oxides. *J. Europ. Ceram. Soc.* **2018**, *38*, 3578–3584. [CrossRef]
41. Sarkar, A.; Loho, C.; Velasco, L.; Thomas, T.; Bhattacharya, S.S.; Hahn, H.; Djenadic, R. Multicomponent equiatomic rare earth oxides with a narrow band gap and associated praseodymium multivalency. *Dalton Trans.* **2017**, *46*, 12167–12176. [CrossRef]
42. Akrami, S.; Edalati, P.; Fuji, M.; Edalati, K. High Entropy Ceramics: Review of principles, production, and applications. *Mater. Sci. Eng.* **2021**, *146*, 100644. [CrossRef]
43. Ermakova, L.V.; Zhuravlev, V.D.; Khaliullin, S.M.; Vovkotrub, E.G. Thermal analysis of the products of SCS of zinc nitrate with glycine and citric acid. *Thermochim. Acta* **2021**, *695*, 178809. [CrossRef]
44. Zhuravlev, V.D.; Ermakova, L.V.; Khaliullin, S.M.; Bamburov, V.G.; Patrusheva, T.A.; Porotnikova, N.M. Features of Copper(II) Oxide Synthesis in Combustion Reactions with Glycine and Citric Acid. Rus. *J. Inorg Chem.* **2022**, *67*, 790–798. [CrossRef]
45. Shannon, R.D. Revised effective ionic radii and systematic studies of interatomic distances in halides and chalcogenides. *Acta Cryst.* **1976**, *A32*, 751–767. [CrossRef]
46. Roth, R.S.; Schneider, S.J. Phase Equilibria in Systems Involving the Rare-Earth Oxides. Part I. Polymorphism of the Oxides of the Trivalent Rare-Earth Ions. *J. Res. NBS* **1960**, *64*, 309. [CrossRef] [PubMed]

47. Warshaw, J.; Roy, R. Polymorphism of the rare earth srsquioxides. *J. Phys. Chem.* **1961**, *65*, 2048–2051. [CrossRef]
48. Shlyakhtina, A.V.; Vorobieva, G.A.; Shchegolikhin, A.N.; Leonov, A.V.; Kolbanev, I.V.; Streletskii, A.N. Phase Relations and Behavior of Carbon-Containing Impurities in Ceramics Prepared from Mechanically Activated $Ln_2O_3$ + $2HfO_2$ (Ln = Nd, Dy) Mixtures. *Inorg. Mater.* **2020**, *56*, 528–542. [CrossRef]